



Core-shell hetero-nanostructured 1D transition metal polyphosphates decorated 2D bimetallic layered double hydroxide for sustainable hybrid supercapacitor

Swati J. Patil^{a,b}, Nilesh R. Chodankar^b, Rahul B. Pujari^a, Young-Kyu Han^b, Dong Weon Lee^{a,c,*}

^a MEMS and Nanotechnology Laboratory, School of Mechanical Engineering, Chonnam National University, Gwangju, 61186, Republic of Korea

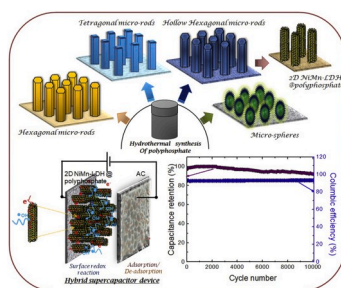
^b Department of Energy and Materials Engineering, Dongguk University-Seoul, Seoul, 04620, Republic of Korea

^c Center for Next-generation Sensor Research and Development, Chonnam National University, Gwangju, 61186, Republic of Korea

HIGHLIGHTS

- Vertically aligned 2D-NiMn-LDH@1D-polyphosphate core-shell structure is prepared.
- 2D-NiMn-LDH@1D-polyphosphate exhibits specific capacity of 662.95 mAh g⁻¹.
- Assembled hybrid supercapacitor delivers specific energy of 56.15 Wh kg⁻¹.
- The hybrid supercapacitor endured superior cyclic stability over 10000 cycles.

GRAPHICAL ABSTRACT



ARTICLE INFO

Keywords:

1D polyphosphate
2D NiMn-Layered double hydroxide
Hexagonal microrods
Nanoflakes

ABSTRACT

In this work, a hierarchical 2D NiMn-layered double hydroxide (LDH) @1D transition metal polyphosphates (1D NiCoP₂O₇) nanostructure is rationally prepared for hybrid sustainable supercapacitor to overcome the limitation of the traditional carbon-based supercapacitor. Initially, the vertically aligned 1D NiCoP₂O₇ hexagonal microrods are prepared over 3D nickel foam and then it is decorated with 2D NiMn-LDH nanoflakes to form core-shell nanostructure. Benefiting from the micro-nano structure, 2D NiMn-LDH@NiCoP₂O₇ core-shell electrode exhibits excellent electrochemical features with reversible charge storage specific capacity of 662.95 mAh g⁻¹ and excellent rate capability, which is quite suitable for the high-energy hybrid supercapacitor fabrication. The accumulated hybrid supercapacitor consisting of 2D NiMn-LDH@NiCoP₂O₇ and activated carbon achieves a high specific capacitance of 142.1 F g⁻¹, delivers remarkable specific energy (56.15 Wh kg⁻¹ at a specific power of 4210 W kg⁻¹) and endured superior cyclic stability over 10000 cycles. Such remarkable results may provide a new perspective for the development of supercapacitive electrode from metal oxide materials.

* Corresponding author. MEMS and Nanotechnology Laboratory, School of Mechanical Engineering, Chonnam National University, Gwangju, 61186, Republic of Korea.

E-mail address: mems@jnu.ac.kr (D.W. Lee).

<https://doi.org/10.1016/j.jpowsour.2020.228286>

Received 14 February 2020; Received in revised form 17 April 2020; Accepted 28 April 2020

Available online 17 May 2020

0378-7753/© 2020 Elsevier B.V. All rights reserved.

1. Introduction

Over the past few years, research has been conducted on a hybrid supercapacitor (SCs) as state-of-the-art to overcome the limitations of the traditional carbon-based SCs. With tangible advantages of rapid charge/discharge activity, high power density, prolonged lifetime and pollution-free operation, SCs are considered as an encouraging power source for various advanced portable technologies [1,2]. A hybrid SCs consists of two distinct electrodes, which have capacitive (as the power source) and battery-type charge storage (as the energy source) functions. The battery-type electrode materials can store many charges than the traditional carbon based electrical double-layer capacitors (capacitive type-materials), which is due to the redox-active behavior. However, the lower cycle lifespan and limited rate capability of battery-type materials keeping constraints on the resultant electrochemical performance of the SCs cell. Thus, combining the battery-type and capacitive charge storing materials in the single-cell with asymmetric design could maintain the rate capability and securing the cycling stability of the SCs device [3,4].

The transition metal pyrophosphates ($M_2P_2O_7$) are the hottest electroactive material that has shown great potential in the field of catalysts and energy storage due to their extensive working potential limit, redox-active, good reversibility, high conductivity, stable layered structure, naturally abundant and inexpensive [5,6]. In which, $M = Ni, Co, Mn$ materials have a struvite-type orthorhombic structure. So far, various transition metal polyphosphates including micro/nanostructured $Mn_2P_2O_7$, amorphous $Ni_2P_2O_7$, $Ni_2P_2O_7$ micro-sheets, and $Ni_xCo_{2-x}P_2O_7$, as well as microflower-like $Co_2P_2O_7$ have been fabricated as electrode materials in SCs [5,7–11]. However, pyrophosphates usually bestowed confined kinetics throughout the redox reaction as a consequence of their feeble electrical conductivities and moderately small surface areas. Therefore, the performance of the electrode materials restricted with their metal compositions. It is a good convincing assurance that the cobalt-nickel hybrid oxide has a synergistic effect between nickel and cobalt species to improve electromechanical performance [12]. To greet the aforementioned detriments and knocks their electrochemical performances, herein, we have proposed the bimetallic functional polyphosphates with varying the composition ratio and optimizing the corresponding changes in behavior. Besides, a new concept is emerging for the smart hybridization of the porous nanostructure have grown on Ni-foam as highly conductive and rigid self-assembling matrices, so it is conceivable to prepare self-adhesive electrodes without using conductive additives or polymer binders that have greatly contributed to the improvement of electrochemical characteristics.

As a result, to meet the obligations of high specific capacity, long-term structural stability, and to encourage the comprehensive use of active materials to the SC electrode, the approach involves the precise design of nano-architectural electrodes and the hybridization of redox-active oxides. The repetitive layered structure of layered double hydroxide (LDH) composed of metal cations, interlayer anions and hydroxyl groups have more advantages due to the abundant redox reaction between bimetallic ions, porous and unique lamellar structure and its vast compatibility [13,14]. The LDH nanoflakes along with hexagonal microrods will noticeably improve the number of exposed electrochemically active sites, which will considerably enhance the ion diffusion efficiency during the reversible electrochemical reactions [15]. There is a possibility to enhance the energy density of the SCs by tuning the porosity of the active material that should be lower than the hydrodynamic size of the active ion, equivalent, or higher than the desolated ions [16]. This porous nature of the active material will help to reduce the rate of discharging hereby enhancing the energy density of SCs.

The intention of the aforementioned design hetero-nanostructure is effectively employed both core and shell layered materials serve to enhance the capacity of the electrodes. Interestingly, when estimated as cathode for SC, 2D NiMn-LDH @ polyphosphates core-shell hybrid electrode delivers a great specific capacity of $662.95 \text{ mAh g}^{-1}$ at a scan

rate of 2 mV s^{-1} . In this work, 2D NiMn-LDH @ polyphosphates based hybrid SC device is assembled utilizing the activated carbon and aqueous electrolyte, designating the potential candidate for energy storage applications in portable electronic devices.

2. Results and discussion

In present work, to enhance the energy storing capacity of the SCs, we developed a binder-free hetero-nanostructure hybrid polyphosphates-LDH hybrid SC electrode that can be easily integrated with current collector and future energy generation technologies. To obtain the well-arranged core of the polyphosphates hexagonal microrods, the cation compositions ($Ni^{2+}:Co^{2+}$) were changed that may lead to more metal ions infused into microrods of the material. Scheme 1 illustrates the hydrothermal preparation of different microstructures of the polyphosphate electrodes. Initially, hexagonal microrods were grown vertically on Ni-foam without any Ni and Co precursor solution using hydrothermal process. In the hydrothermal process, Ni^{2+} and Co^{2+} cations are hexa-coordinate with urea, and the ligand condition of the cation led to the formation of the hexagonal microrods of the polyphosphates. Afterward, varying the Ni/Co precursor concentration ratio the microrod face changed from hexagonal to tetragonal (1/1), hollow hexagonal microrods (2/1) and micro-spheres (1/2). Ni^{2+} and Co^{2+} cations are tetragonally co-ordinated with urea and phosphate group and the tetragonal faced microrods were directly obtained on Ni-foam. Hollow hexagonal faced microrods as seen in schematic were visualized with hexa-coordinated Ni^{2+} and Co^{2+} cation with urea at 160°C for 10 h hydrothermal process. The micro-spherical surface structure formed with double of Co cation precursor solution may be due to the isometric coordination of the Ni-Co with urea as a complex agent. With controlling the hydrothermal process, the secondary hydrothermal route was further conducted to obtain core-shell structure on Hollow Hexagonal microrods of the polyphosphate electrode. Finally, 2D NiMn-LDH@polyphosphate core-shell electrode was used for the fabrication of hybrid SC devices. Inset right top represents the hybrid SC device based on 2D NiMn-LDH @ polyphosphate (Hollow hexagonal microrods) core-shell and activated carbon as a electrodes with aqueous electrolyte and their charge storage mechanism.

2.1. Morphology and structure analysis

The morphologies and microstructures of the obtained samples were captured by scanning electron microscopy (SEM) and transmission electron microscopy (TEM). The morphological images of the polyphosphates with different ratios of $Ni^{2+}:Co^{2+}$ precursor concentrations are displayed in Fig. 1. The samples were noted as PO00, PO01, PO10, PO1, PO2 and PO3 with $Ni^{2+}:Co^{2+}$ precursor solution ratio of 0:0, 0:1, 1:0, 1:1, 2:1 and 1:2, respectively. Fig. 1(a–c) displays the SEM micrographs of the PO00, PO01 and PO10 polyphosphates samples exhibit hexagonal-shaped 1D microrods structure with the hexagonal faced surface. The faces of the 1D microrod have an average face-length of 300–350 nm while side length lies in micron for PO00, PO01 and PO02 polyphosphate samples. Further, varying the composition ratio of the Ni: Co (PO1), the polyphosphate microstructure turns into tetragonal faced microrod with face length of 400 nm as displays in Fig. 1(d). The SEM images of the as-prepared polyphosphates (PO2) show the distinct hollow tubular hexagonal 1D microrods-like structures and it is successfully observed in Fig. 1(e) on Ni-foam. As a result, compact agglomerated microspheres were observed when the elemental composition of Ni^{2+} and Co^{2+} is settled as 1:2 (PO3) (Fig. 1(f)). Compared with 1D hexagonal microrods, tetragonal microrods, and micro-spheres, hollow tubular hexagonal microrods consist of more attractive surface morphology that may useful for electrochemical application due to the more active surface available insight the microrods. The well covered and uniformly, -arranged unidirectional surface microstructures of the all samples are provided in the supplementary data in Fig. S1 at low

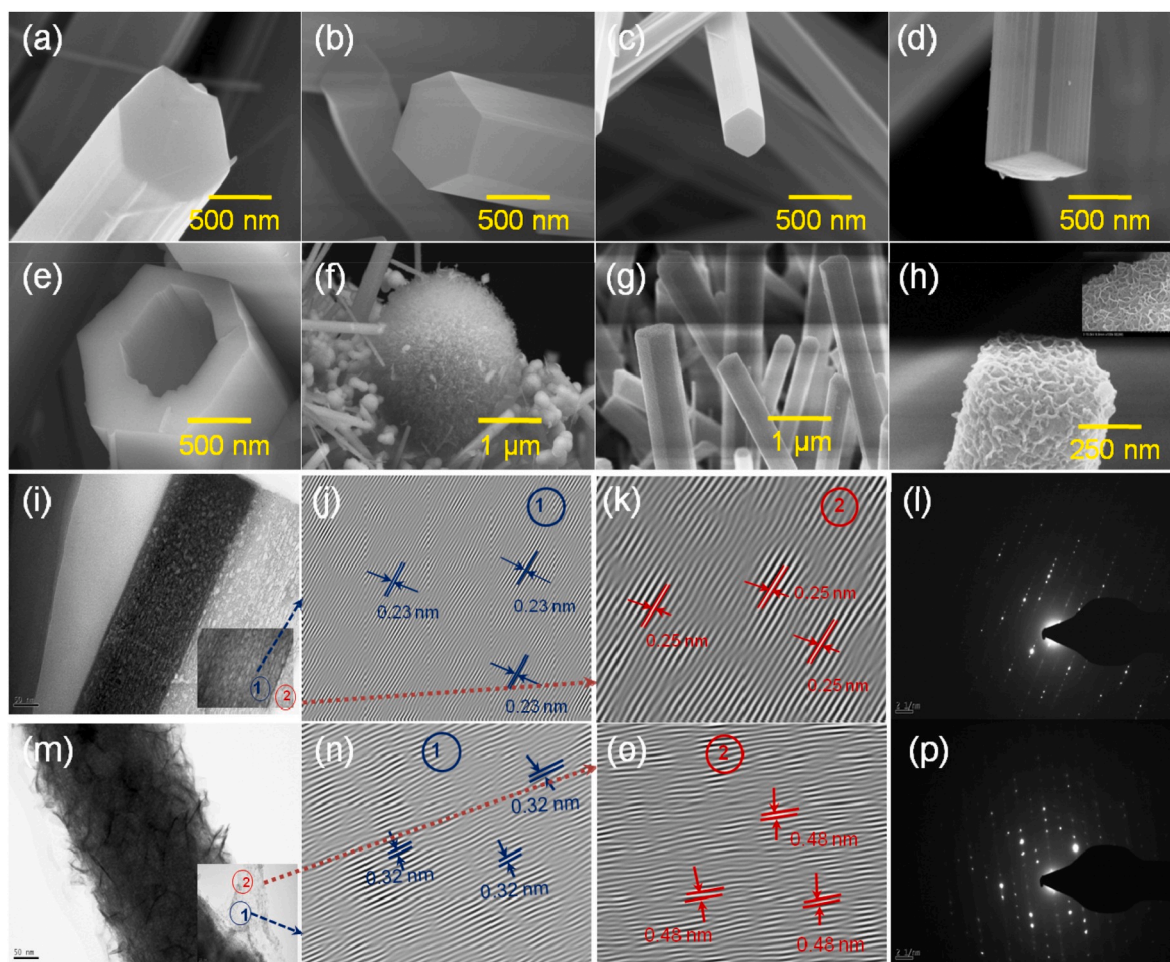
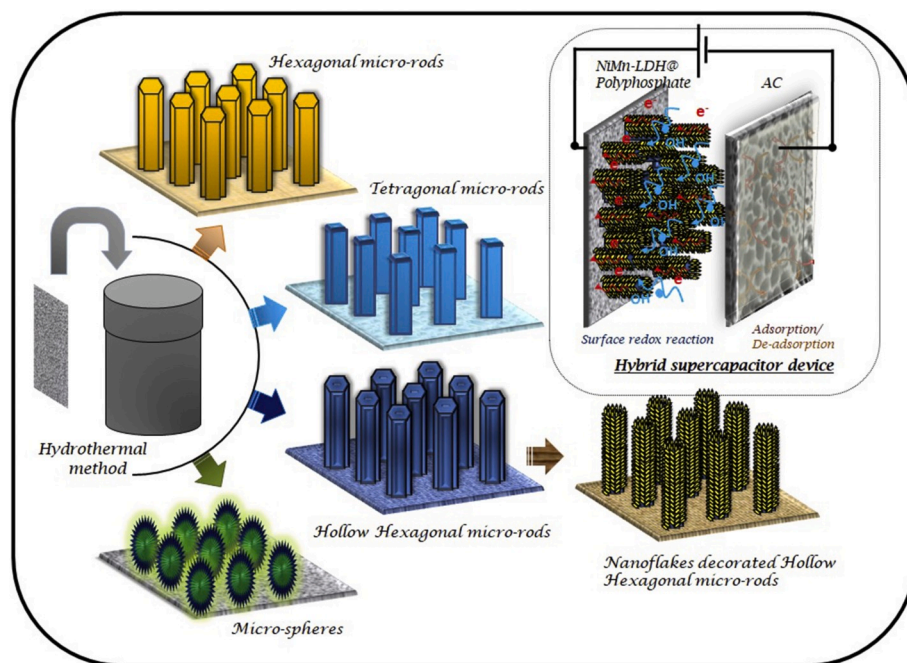


Fig. 1. FE-SEM images of hybrid polyphosphates (a) PO00, (b) PO10, (c) PO01, (d) PO1, (e) PO2, (f) PO3 core samples and (g, h) 2D NiMn-LDH @ polyphosphates (PO4) core-shell sample. TEM images of (i–k) polyphosphates (PO2) and (m–o) 2D NiMn-LDH @ polyphosphates core-shell (inset bottom shows the HR TEM images). (l, p) SEAD pattern of the polyphosphates (PO2) and 2D NiMn-LDH @ polyphosphates samples.

magnifications. From all these Figures, it is seen that the surface microstructure of the prepared samples was changed with altering the Ni:Co precursor composition ratio. The elemental composition of all samples is provided in the supplementary data in Fig. S2. The hollow tubular hexagonal 1D microrod structures will provide high active sites with centered hollows tube. However, the outside surface of the 1D microrod is a bit compact to restrict the electrochemical kinetics during redox processing and electrolyte ion penetration. Therefore, it is necessary to modify the surface of the 1D microrods with loading the heteronanostructure to form the hierarchical core-shell architecture of the electrode. Thus, such a strategy was applied to improve the specific capacity and rate capability of the polyphosphates electrode. 2D NiMn-LDH nanoflakes as a shell are uniformly grown on hollow hexagonal microrod. The high-magnified surface micrograph of the hybrid 2D NiMn-LDH @ polyphosphates (PO4) as represented in Fig. 1(g and h). Moreover, without distortion of the hexagonal microrod, 2D NiMn-LDH nanoflakes were uniformly coated on the microrods. Inset top shows the nanoflakes surface architecture of the 2D NiMn-LDH material. The porous nanoflakes make intimate contact with the electrode surface and provide more electroactive areas for a redox reaction, which is beneficial to the transportation of ion/electrolyte [17].

To further clarify the core-shell heteronanostructure of electrodeposited 2D NiMn-LDH@ polyphosphates sample, TEM analysis was conducted. Fig. 1(i–k) and (m–o) exhibit the TEM images of the polyphosphates and 2D NiMn-LDH @ polyphosphates samples, respectively. It clearly illustrates that hexagonal microrods of polyphosphates core are tightly wrapped with thin nanoflakes of 2D NiMn-LDH as presented in good agreement with the FE-SEM results. Thin nanoflakes are strongly connected to microrods that would provide a convenient ion-transfer pathway for effective electrochemical reactions. High-resolution TEM images of the polyphosphates (PO₂₁) and 2D NiMn-LDH @ polyphosphates are presented inset of Fig. 1(l, m). The magnified parts of the HR-TEM images at points 1 and 2 are shown in Fig. 1(j and k) for polyphosphates, respectively. It demonstrates the commonly observed lattice fringes with the spacing of 0.23 nm corresponding to the (023) plane of NiCoP₄O₁₂ (Fig. 1(j)) and 0.25 nm corresponding to the (130) plane of NiCoP₂O₇ (Fig. 1(k)). While the lattice fringes are shown in Fig. 1(n and o) for the 2D NiMn-LDH @ polyphosphates are the characteristics of 2D NiMn-LDH with an interplanar spacing distance of 0.32 and 0.48 nm corresponds to the (003) and (002) plane of NiMn-hydroxide (NiMn(OH)₄·H₂O). The selected area electron diffraction (SAED) patterns of the polyphosphates and 2D NiMn-LDH @ polyphosphates in Fig. 1(l) and (p) show well-defined diffraction rings, suggesting its polycrystalline characteristics.

Further, the elemental compositions of polyphosphates and their core-shell 2D NiMn-LDH @ polyphosphates heteronanostructure sample can be confirmed by energy-dispersive X-ray spectrometer (EDX) spectra

that were collected in the core and shell regions separately as shown in Fig. 2 (a). To distinguish core and shell similar Ni element presents in the sample, the profiles in the energy region between 6.5 keV and 8.5 keV are magnified inset of the plot. The center region consists of Ni, Co, P, and O, while in additional Mn element was presents in shell region. However, the obtained ratio cannot be accurate due to the overlapping of metal elemental peaks. For the polyphosphates microrod, Ni K_α (7.989 keV), Ni K_β (8.313 keV), Co K_α (7.424 keV), Co K_β (7.525 keV), P K_β (2.011 keV) peaks are detected. For the 2D NiMn-LDH @ polyphosphates core-shell, additional Mn K_α (6.843 keV) and Mn K_β (6.952 keV) peaks appear in the spectrum.

The structural phase formation of the samples further examined by X-ray diffraction (XRD) with monochromatic Cu K_α radiation ($\lambda = 0.154$ nm) at a scanning rate of 10 °C min⁻¹. The phase and structures of the prepared nanostructure samples were investigated by X-ray diffraction (XRD) to ensure the phase composition of the materials. XRD patterns of polyphosphates based samples are shown in Fig. S5. The observed all diffraction peaks of the core material with different Ni²⁺: Co²⁺ precursor concentrations, it can be indexed to be a mixed monoclinic structure of the NiCoP₂O₇ and CoNiP₄O₁₂ phase. The major high intense peaks at 44.45°, 51.78° and 76.35° in all of the prepared samples assigned to be to (111), (200) and (220) planes of Ni (JCPDS #00-004-0850). The peaks at 29.66°, 30.15° and 35.34° in all of these samples are corresponding to (012), (210) and (130) planes of the Monoclinic structure of the NiCoP₂O₇ (JCPDS #00-048-0563). Besides, the major peaks observed at 20.45°, 28.15°, 34.83° and 41.30° are attributed to the (002), (310), (400), and (−511) planes of NiCoP₄O₁₄ (JCPDS #01-076-2283). The peaks further observed indicating the mixed phase of NiP, Co(PO₃)₂ and Ni(PO₃)₂ exist in samples. XRD pattern of 2D NiMn-LDH@ polyphosphates sample, in addition to the peaks referring to the NiCoP₂O₇ and CoNiP₄O₁₂, the diffraction peaks at 60.01° and 65.65° belongs to (302) and (220) planes of NiMnO₃(OH)₄·H₂O phase (JCPDS #00-042-1319), while the peaks appear at 25.87°, 36.75°, 37.76°, and 48.26° related to (015), (211), (122), and (217) plan of the NiMn-Hydroxide (JCPDS #00-046-1476). From these results confirmed the formation of 2D NiMn-LDH@ polyphosphates architecture on the Ni-foam.

Latterly, the chemical composition and metal oxidation states of the polyphosphates and 2D NiMn-LDH @ polyphosphates core-shell heteronanostructure were detected by X-ray photoelectron spectra (XPS) and results are presented in Fig. 3(a–f) and Fig. S6. The fitted peaks of Ni 2p, Co 2p, P 2p, Mn 2p and O 1s are orbital's as shown in Fig. 3(b–f) as identified from the full scan spectrum on the core-shell hetero-nanostructure of the material. The peaks at 853.2 eV and 870.6 eV (Fig. 3(b)) can be ascribed to the 2p_{3/2} and 2p_{1/2} states of Ni²⁺, and the peaks at 856.05 eV and 875.01 eV correspond to the 2p_{3/2} and 2p_{1/2} states of Ni³⁺, suggesting the co-existence of Ni³⁺ and Ni²⁺ [18]. The Co 2p spectrum in Fig. 3(c) can be fitted as two major binding energies of Co

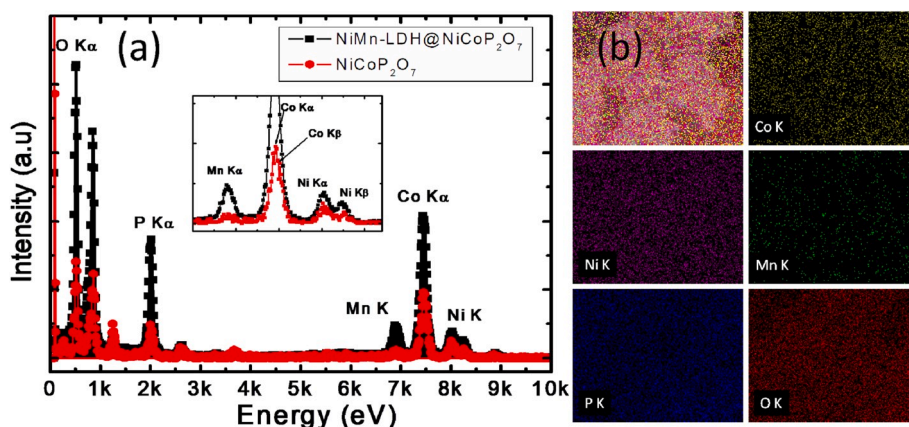


Fig. 2. (a) EDX spectra of polyphosphates and 2D NiMn-LDH @ polyphosphates core-shell electrode. Inset shows the magnified signal of the Mn, Co and Ni K elements. (b) Elemental mapping images of the Co, Ni, Mn, P, and O in the 2D NiMn-LDH @ polyphosphates core-shell nanostructure.

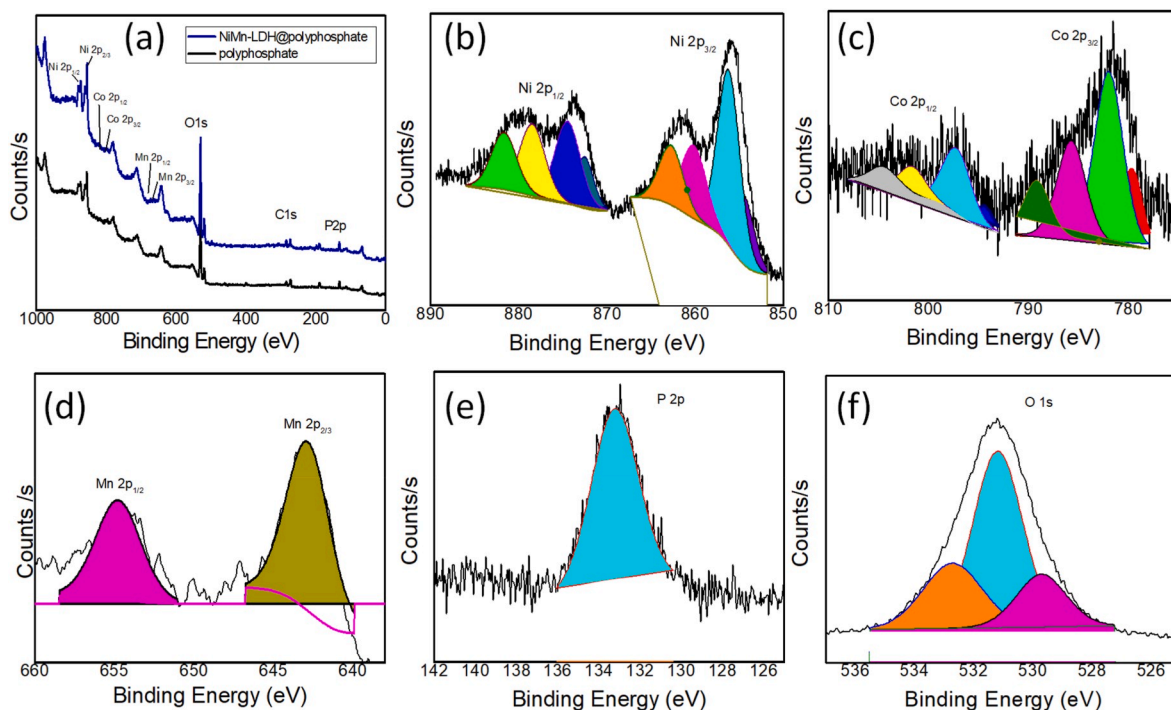


Fig. 3. (a) The wide XPS spectra of polyphosphates and 2D NiMn-LDH @ polyphosphates core-shell heteronanostructure. Deconvoluted high-resolution (b) Ni 2p, (c) Co 2p, (d) Mn 2p, (e) P 2p, and (f) O 1s of 2D NiMn-LDH @ polyphosphates core-shell heteronanostructure.

$2p_{1/2}$ at 796.62 eV and $Co 2p_{3/2}$ at 777.80 eV along with two satellite peaks which can be identified as Co^{2+} [19]. For the Mn 2p spectrum, two strong peaks at around 642.9 and 654.7 eV (Fig. 3(d)) are assigned to Mn $2p_{1/2}$ and Mn $2p_{3/2}$, revealing the binding energy of the Mn^{2+} ions in the obtained 2D NiMn-LDH @ polyphosphates core-shell [20]. For the P 2p core-level spectrum, the main peak has occurred at a binding energy of

132.54 eV, which mainly owing to the P-O bonds [21] as seen in Fig. 3 (e). The fitted high resolved O 1s spectrum shows three oxygen contributions as represented in Fig. 3(f). The strong XPS peak centered from 529.6 eV could be assigned to oxygen atoms in the oxides of 2D NiMn-LDH and polyphosphates core-shell hetero-nanostructure [22]. The typical binding energies of 531.02 and 532.7 eV are usually

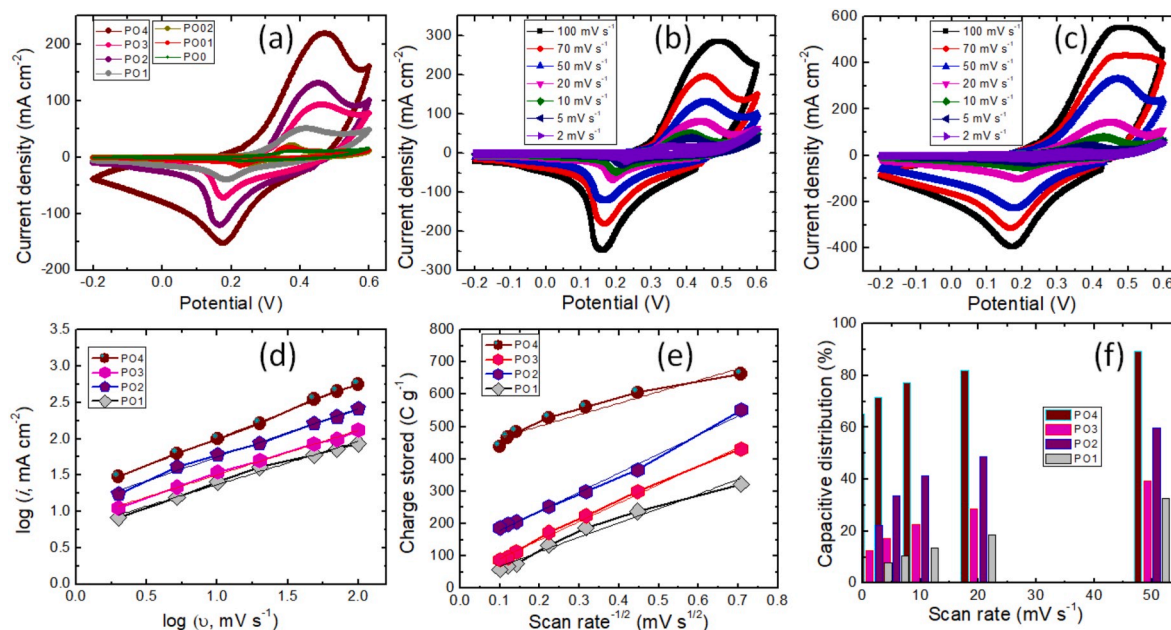
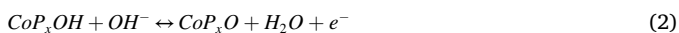


Fig. 4. (a) The comparative cyclic voltammetry curves of a hybrid 2D NiMn-LDH @ polyphosphates core-shell electrode using three-electrode at scan rates of 50 $mV s^{-1}$. (b, c) shows the cyclic voltammetry curves of (b) polyphosphates, and (c) 2D NiMn-LDH @ polyphosphates core-shell electrode in the scanning range from 2 $mV s^{-1}$ up to 100 $mV s^{-1}$. (d–f) Kinetic analysis of the polyphosphates and 2D NiMn-LDH @ polyphosphates core-shell electrode: (d) determination of b-values from the i_p Vs logarithmic scan rate plot at different scan rates. (e) The specific capacity as a function of the square root of scan rate for the hybrid polyphosphates and its core-shell based electrodes. Pseudocapacitive contribution calculated from the total charge storage in percentage at different scan rates for selected polyphosphates based electrodes.

associated with oxygen in OH⁻ groups and multiplicity of physi- and chemisorbed water at or near the surface, respectively [23].

2.2. Electrochemical characterizations and kinetic analyses of the electrodes

All electrochemical measurements including cyclic voltammograms (CV), galvanostatic charge/discharge (GCD) curves of polyphosphates and its 2D NiMn-LDH @ polyphosphates core-shell hetero-nanostructure electrode were carried out using electrochemical workstation (IVIUM Tech). Electrochemical impedance spectra (EIS) measurements were performed in the frequency range from 1 MHz to 0.1 Hz at open circuit potential with an AC perturbation of 10 mV. To study the benefits of the electroactive ions in SC electrode material, the electrochemical properties of the polyphosphates based core-shell hetero-nanostructure SC electrodes (PO0, PO01, PO02, PO1, PO2, PO3 and PO4) were conducted in the constant potential range between -0.2 and 0.6 V and 50 mV s⁻¹ scan rates as summarized in Fig. 4(a). The electrochemical CV profiles with different scanning rates for polyphosphates based different electrodes were provided in the data of Supplementary information (Fig. S7). Compared to pristine polyphosphates with different Ni to Co precursor solution concentration ratio, polyphosphates (PO2) shows better electrochemical activities due to the favors of two cation that limit deficient to fast electron transport and relatively confine the electrochemical cyclic stability [24]. Meanwhile, binary to ternary coupling gives somewhat electroactive species and tremendous interest to overcome the shortage of conductivity and contributes to improving the electrochemical cyclic stability performance [25]. Thus, it is used as a core electrode and further 2D NiMn-LDH @ polyphosphates showing excellent redox activities. Transition metals such as; nickel (Ni), cobalt (Co), manganese (Mn), etc. have been believable for electrochemical studies possessing extraordinary features and richer redox activities. The main pair of redox reaction peaks shown in Fig. 4(a) was due to the reversible redox reaction between the electrode material and electrolyte ions from the electrolyte as explained using the following equation [26];



The separate CV profile of polyphosphates and 2D NiMn-LDH @ polyphosphates electrodes are illustrated in Fig. 4(b) and (c) at scanning rates from 2 to 100 mV s⁻¹. It is seen that area under the CV curve of 2D NiMn-LDH @ polyphosphates electrode improved with the formation of 2D NiMn-LDH shell over the polyphosphates core electrode. The charge storage mechanism in the electrode having two types of relative contributions, i) the pseudo-capacitive type and ii) diffusion-controlled battery-type processes to the total charge storage. These contributions further analyzed according to power-law relation (equation (3)) for a better understanding;

$$i_p = av^b \quad (3)$$

where, i_p is the peak current density in a CV curve at different scan rates (v), a and b are adjustable parameters. In which, the values of b equal 1, the response current is proportional to the scan rate, indicating a capacitive process. Whereas if b -value equals to 0.5, the response current satisfies Cottrell's equation, reflecting a diffusion-controlled process [27,28]. The fitting plots displayed in Fig. 4(d) exhibits that logarithm i_p is linear with logarithm v , and the b values determined from the slope of the curve. The calculated b -values are 0.75, 0.59, 0.67, and 0.62 for 2D NiMn-LDH @ polyphosphates (PO4), PO1, PO2, and PO3 in polyphosphates electrodes, respectively realizes that the semi-infinite diffusion-controlled processes and the capacitive surface mechanism exist in the polyphosphates based electrodes. Fig. 4(e) illustrates the total specific capacity as a function of the square root of the scanning rate that can be used to better resolve low scan rate behavior. From these results,

it is confirmed that the specific capacity of the 2D NiMn-LDH @ polyphosphates core-shell electrode has more charge storage capability than the pristine polyphosphates based electrodes at different composition ratios of Ni:Co. Further, to analyze the relative charge storage contributions from the current response at the certain scan rate, the following equation used to quantify the pseudocapacitive and diffusion-controlled processes in the electrode material [29],

$$i = k_1v + k_2v^{1/2} \quad (4)$$

where, k_1v and $k_2v^{1/2}$ are the pseudo-capacitive and diffusion-controlled related processes, respectively. Fig. 4(f) summarizes the relative capacitive contributions of the electrodes at lower the scan rates, indicating the diffusion-controlled processes predominate, while at the higher scan rate, the pseudo-capacitive contribution surpassing. In the case of 2D NiMn-LDH @ polyphosphates core-shell electrode, pseudo-capacitive processes are more predominant due to the well synergistic consequence of engineering the core-shell hetero-nanostructure for the plentiful active sites and subsequence massive surface area for achieving prominent electrochemical feature [30].

The electrochemical performances of the prepared electrodes were further examined by galvanostatic charge/discharge measurements. The comparative charge-discharge profiles of hybrid polyphosphates and its 2D NiMn-LDH core-shell electrode at different current densities are displayed in Fig. 5(a-d). The charge/discharge profiles for the PO00, PO1 and PO3 polyphosphates electrode with various current densities are provided in Fig. S8. 2D NiMn-LDH @ polyphosphates core-shell electrode exhibits the longest discharge time and the surface controlled diffusion processes occurring at the interface of electrode/electrolyte. Moreover, the specific capacity versus current densities plot as demonstrated in Fig. 5(d). The specific capacity of the electrode decreased with increasing the current density as seen in the plot that associated with the prolonged diffusion suppression. The specific capacity value of hybrid polyphosphates core-shell is 394.45 mA h g⁻¹ for 2D NiMn-LDH @ polyphosphates core-shell (PO4) which is higher than polyphosphates based electrodes such as, 102.31 mA h g⁻¹ for PO1, 210.20 mA h g⁻¹ for PO2, and 131.20 mA h g⁻¹ for PO3 electrodes. 2D NiMn-LDH @ polyphosphates core-shell heteronanostructure demonstrates high specific capacity due to the hierarchical structure of the double layer of the NiMn-hydroxides that not only provide the abundant convenient active sites but also enhances the ion diffusion and electron transfer rate between the electrodes and electrolytes. The specific rate capacity of core-shell electrode further determined, the nanoflakes wrapped 2D NiMn-LDH on polyphosphates microrods shows excellent rate performance of ~65% with increasing the current density of 6 times higher which is more better than polyphosphates (PO0 ~18.7%). The open geometry including polyphosphates hollow microstructure core and 2D NiMn-LDH nanoflakes shell allowed slight invasion of electrolyte ion within the interior zone of the core-shell electrode that ameliorating the electrochemical performance through utilizing the extra active surface area of the materials. The cyclic stability of the 2D NiMn-LDH @ polyphosphates and polyphosphates electrode were carried out over 5000 cycles (Fig. S9). In addition, 2D NiMn-LDH on polyphosphates microrods (92.45%) exhibits superior cyclic stability than the polyphosphates (81.52%) electrode over 2000 charge/discharge cycles. It indicates that the core-shell hetero-nanostructure not only secures the stability of the core material, as well as enhances the rate capability.

Impedance spectra judgment is like wisely employed on a significant aspect for quantitatively estimating the electrical resistance and electrochemical performance characteristics of the polyphosphates and 2D NiMn-LDH @ polyphosphates core-shell electrodes in the frequency range of 100 kHz to 0.1 Hz. Nyquist plots as seen in Fig. 5(e), the distinct part is composited of two regions (i) the curvature in the high-frequency region and (ii) the presence of a straight line in the low-frequency region. According to the recorded spectra of the sample electrodes, the fitting processes were employed to obtain the best match equivalent

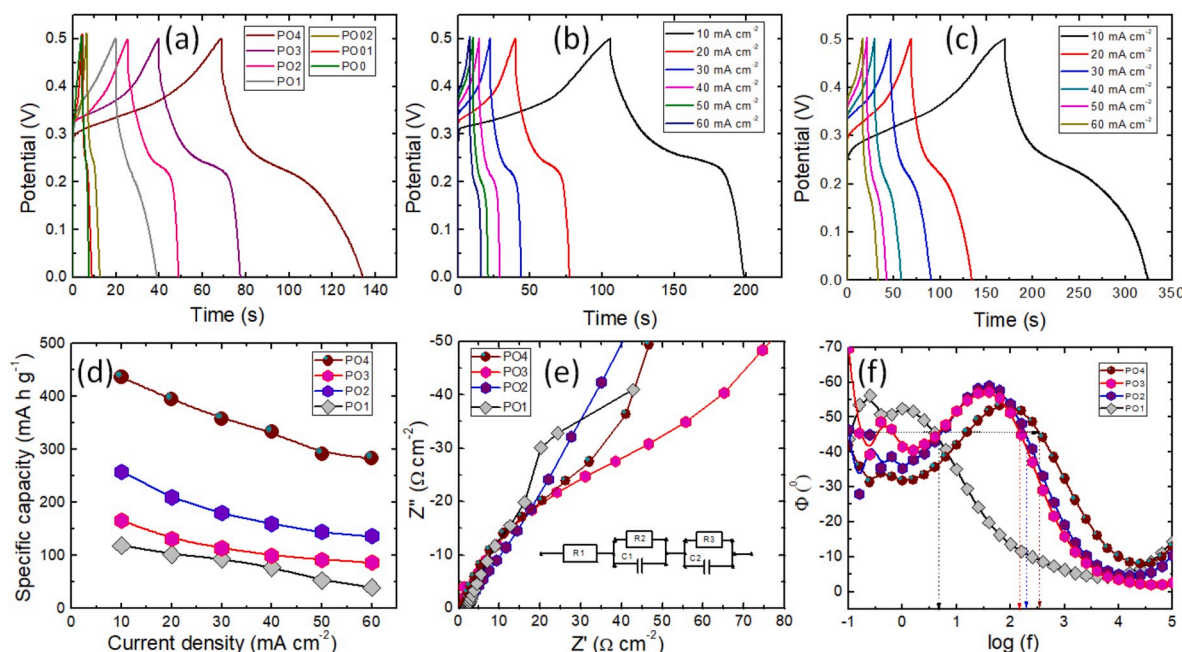


Fig. 5. (a) The comparative galvanostatic charge/discharge curves of the prepared polyphosphates electrodes under a constant current density of 20 mA cm^{-2} (b-d). The separate charge/discharge curves for (b) polyphosphates and (c) 2D NiMn-LDH @ polyphosphates core-shell electrodes. (d) The calculated specific capacities of the polyphosphates electrodes at current densities from 10 to 60 mA cm^{-2} . Impedance analyses of the polyphosphates based electrodes; (e) Nyquist plot, (f) Phase angle plot.

circuit. From the fitting circuit, solution resistance values were estimated for 2D NiMn-LDH @ polyphosphates core-shell electrode (PO4): 1.26Ω which is lower than the PO1 (1.8Ω), PO2 (1.32Ω) and PO3 (1.48Ω) of polyphosphates electrode and further corresponding relaxation time constant calculated to be 1.58 (632 Hz), 6.25 (125 Hz), 8.0 (160 Hz) and 158 ms (63.1 Hz), respectively from the Bode plot (Fig. 5(f)). 2D NiMn-LDH @ polyphosphates core-shell electrode tends the phase angle of -90° shows the excellent capacitive behavior. In addition, the steeply oblique line at the low-frequency region implies that the core-shell electrode exposes fast electrolyte ion diffusion rate during the charge/discharge processes. To recap, the steeply oblique line at the low-frequency region clearly illustrate that 2D NiMn-LDH @ polyphosphates core-shell electrode exposes fast electrolyte ion diffusion rate during the charge/discharge processes encouraging charge-transfer kinetics and quick electron carrier. Thus, 2D NiMn-LDH @ polyphosphates core-shell electrode promotes dramatically improved capacitive performance compared to the pristine polyphosphates electrode.

2.3. Electrochemical characterization of hybrid supercapacitor device

Enhancing the energy storing capacity of the SCs is required to widen their applicability at the commercial level. With this motivation, researchers are trying to develop the advance electrode materials, electrolytes and cell designs to boost the energy storing capacity of the SCs by keeping its fundamental features. To obtain true electrochemical performance for the prepared core-shell structured electrode, two-electrode system measurements are carried out by assembling the hybrid SCs with 2D NiMn-LDH @ polyphosphates core-shell and AC as a positive and negative electrode in aqueous KOH electrolytes. The details regarding the AC electrode preparation and the hybrid device fabrication are provided in the experimental section. Prior to assembling the hybrid SCs, the charge balancing of the positive and negative electrode is essential to achieve higher voltage limit and energy storing capacity. The charge balancing from the positive to the negative electrode is carried out by adjusting the mass of the negative electrode and corresponding information is provided in the experimental section. According

to the charge balancing, the mass ratio from the positive to the negative electrode is 0.54 . In three-electrode measurements, the 2D NiMn-LDH @ polyphosphates electrode work in the positive potential range of -0.2 to 0.6 V/SCE , while the AC electrode works in the potential range of -0.9 to 0 V/SCE that indicates an hybrid device with these two electrodes can achieve the voltage limit of 1.6 V . Initially, to optimize the voltage limit for the assembled SC cell the charge/discharge measurements are carried out at various voltage range at a constant current density of 20 mA cm^{-2} and the results indicate the 1.6 V optimized voltage for the SC cell (Supporting info Fig. S11). Fig. 6(a) represents the CV sweeps of the 2D NiMn-LDH @ polyphosphates//AC hybrid device at the scan rates from 2 to 100 mV s^{-1} . The CV curves are recorded inside a voltage range of 0 – 1.6 V , there is no obvious polarization transpires when the potential of the employed positive and negative electrode is greater or less than that of an applied potential in a three-electrode system. Thus, 2D NiMn-LDH @ polyphosphates//AC hybrid device affords the safety and a feasible operation in that given operating voltage range is to be implemented. The shape of the CV curves maintained analogous beside the increment of the scan rate insinuating a fabricated device owned an outstanding rate capability. Fig. 6(b) shows the charge/discharge profiles of the 2D NiMn-LDH @ polyphosphates//AC hybrid SCs device at different current densities recorded from 8 to 20 mA cm^{-2} . The calculated areal and specific capacitances of the 2D NiMn-LDH @ polyphosphates//AC hybrid SCs device are depicted in Fig. 6(c). The specific capacitance of the fabricated hybrid SC device dramatically decreased as the current density increased. The maximum specific capacitance of 157.9 and 142.1 F g^{-1} found to be at 8 and 10 mA cm^{-2} current density, respectively. The fabricated SC device possessed superior capacitance retention of 63% with increased twice the current densities from 10 mA cm^{-2} to 20 mA cm^{-2} . Inset Fig. 6(c) displays the pie diagram represents the rated capacity of the fabricated SC device in percentage. Further, the specific energy and power of the 2D NiMn-LDH @ polyphosphates//AC hybrid SC device were estimated at the different charge/discharge current densities and results illustrated in Fig. 6(d). The specific energy of 2D NiMn-LDH @ polyphosphates//AC hybrid SC can approach 56.15 Wh kg^{-1} at a specific power of 3.37 kW kg^{-1} . Moreover, at a greatly high current density of 20 mA cm^{-2} , it could still perform a high specific

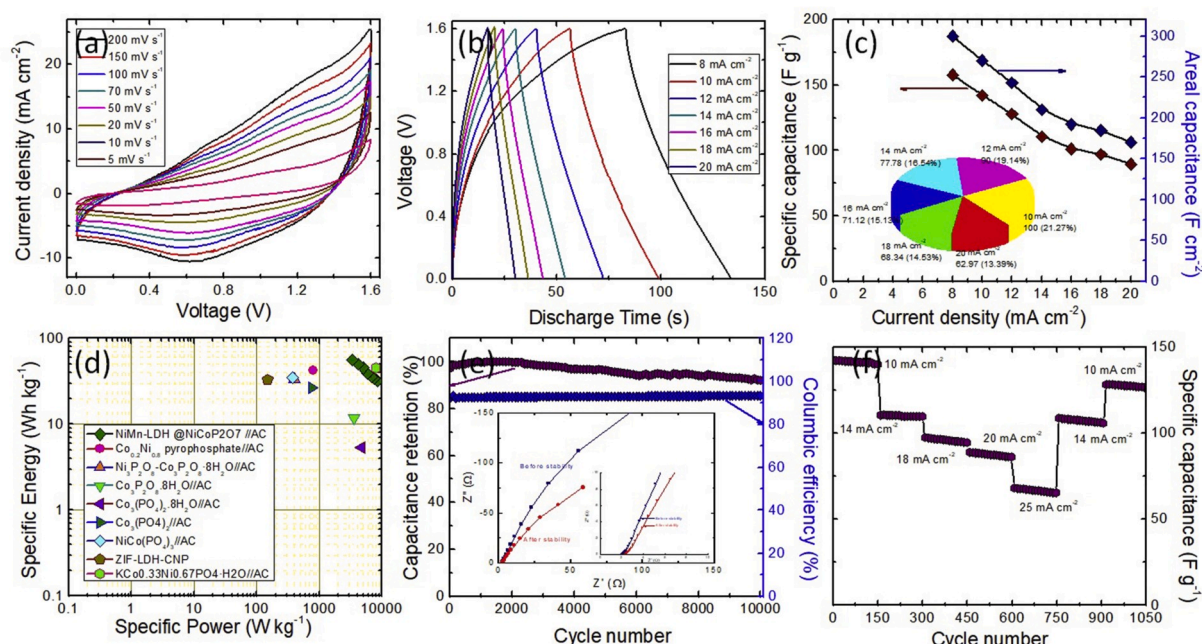


Fig. 6. Electrochemical characteristics of the 2D NiMn-LDH @ polyphosphates//AC hybrid SC device. (a) CV profiles of the fabricated SC device at different scanning rates collected in the voltage range from 0 to 1.6 V. (b) GCD curves of fabricated SC device at various current densities. (c) The plot shows the calculated areal and specific capacitance values with their corresponding current densities. Inset pie diagram displays the rate capacity in percentage with increase in current density. (d) Ragone plot of 2D NiMn-LDH @ polyphosphates//AC hybrid SC device correlated with recently reported asymmetric SCs devices in the literature. (e) The capacitance retention and columbic efficiency versus cycle numbers of 2D NiMn-LDH @ polyphosphates//AC SC device, inset shows the Nyquist plot and its enlarged area at the high frequency region of fabricated SC device before and after 10000 cycling performance. (f) The capacitance rate capability of the 2D NiMn-LDH @ polyphosphates//AC hybrid SC device with lower to higher and reverse back to the current density.

power of 8.43 kW kg⁻¹. Ragone plot of 2D NiMn-LDH @ polyphosphates//AC SC device correlated with very recently reported asymmetric devices in the literature (values of capacitance, energy and power density are provided in Table S1) [31–37]. We assume that proper structure expression strength remains implemented to other electrode materials to reach the optimal electrochemical reaction and kinetic requirements.

Electrochemical cyclic stability is one of the important parts of the energy storage device to operate long-time durability. Therefore, 2D NiMn-LDH @ polyphosphates//AC hybrid SC was tested at a current density of 10 mA cm⁻² and it possesses excellent capacitance retention of 91.13% over 10000 electrochemical charge/discharge cycles. From Fig. 6(e), it is observed that the capacitance retention of the fabricated SCs device increases initially first for 1000 cycles that might be an activation process of the electrodes. Further, increases in cycle numbers occurred attenuation of capacitance may be due to the exfoliation of some active materials from the 2D NiMn-LDH @ polyphosphates electrode [38]. Moreover, 2D NiMn-LDH @ polyphosphates//AC SCs device displays good Columbic efficiency of about 93.35% over 10000 cycles that is beneficial for the high-power applications. The executive pseudocapacitive contribution can be associated with the excellent rate capability referred to the novel core-shell nanostructure of the 2D NiMn-LDH @ polyphosphates electrode. Fig. 6(f) depicts the plot for rate capacities of the 2D NiMn-LDH @ polyphosphates//AC SC device with different current densities indicating excellent rate capability with minimal capacity fading when the charge rate increases from 10 mA cm⁻² to 25 mA cm⁻². The charge capacities of NiMn-LDH @ polyphosphates//AC SC device maintained even after 150 cycles at the current densities of 10, 14, 18, 20 and 25 mA cm⁻², respectively. Moreover, reverse back the current density to the lower scan rate, the capacitance of the 2D NiMn-LDH @ polyphosphates//AC SC device could be recovered nearly its initial capacitance value even after 1050 cycles, implying a recovery ratio of 90.15%. To obtain further insight into the comparable EIS performance of the fabricated SCs device before

and after 10000 stability cycles, EIS measurements were conducted. The Nyquist plots are shown inset of Fig. 6(e). It is observed that obvious relatively large charge transfer resistance of the SC device compared to the before stability cycling. The typical behavior of the Nyquist plot in the lower frequency region titled to the X-axis after cycling. Hence, the phase angle shifted to the lower frequency region and likely relaxation time constant increased as shown in the Phase angle plot provided in supporting data Fig. S12.

3. Conclusions

In summary, we manifested an apparent preparation of unique hierarchically 2D NiMn-LDH @ polyphosphates core-shell nanostructure through a hydrothermal route on Ni foam and investigated their morphological and electrochemical characteristics for hybrid SCs device. The 2D NiMn-LDH @ polyphosphates//AC SC device possessed a specific capacitance of 142.1 F g⁻¹ and delivered a high specific energy density of 56.15 Wh kg⁻¹ at 3.37 kW kg⁻¹ with excellent cycling stability rate performances (91.3%) after 10000 cycles. The obtained results reveal that polyphosphates microstructure with tunable element compositions displays excellent electrochemical behavior towards the redox processes holds micro-structural benefits with 2D NiMn-LDH nanoflakes and electronic synergy for the 2D NiMn-LDH @ polyphosphates. Certain conclusions endorse the potential applicability of the 2D NiMn-LDH @ polyphosphates core-shell nanostructure hybrid electrode in energy storage.

Declaration of competing interest

The authors declare that they have no known competing financial interests or personal relationships that could have appeared to influence the work reported in this paper.

CRediT authorship contribution statement

Swati J. Patil: Conceptualization, Writing - original draft. **Nilesh R. Chodankar:** Writing - review & editing. **Rahul B. Pujari:** Data curation. **Young-Kyu Han:** Validation, Software. **Dong Weon Lee:** Visualization, Supervision, Funding acquisition.

Acknowledgment

This study was supported by the National Research Foundation of Korea (NRF) grant funded by the Korea government (MSIT) (No.2017R1E1A1A01074550) and Chonnam National University (Grant no. 2017-2837).

Appendix A. Supplementary data

Supplementary data to this article can be found online at <https://doi.org/10.1016/j.jpowsour.2020.228286>.

References

- P. Pachfule, D. Shinde, M. Majumder, Q. Xu, Fabrication of carbon nanorods and graphene nanoribbons from a metal-organic framework, *Nat. Chem.* 8 (2016) 718.
- Y. Liu, X. Li, W. Shen, Y. Dai, W. Kou, W. Zheng, X. Jiang, G. He, Multishelled transition metal-based microspheres: synthesis and applications for batteries and supercapacitors, *Small* (2019) 1804737.
- N. Hu, L. Huang, W.H. Gong, P.K. Shen, High-performance asymmetric supercapacitor based on hierarchical $\text{NiMn}_2\text{O}_4/\text{CoS}$ core-shell microspheres and stereotaxically constricted graphene, *ACS Sustain. Chem. Eng.* 6 (2018) 16933–16940.
- W.Q. Chen, J. Wang, K.Y. Ma, M. Li, S.H. Guo, F. Liu, J.P. Cheng, Hierarchical $\text{NiCo}_2\text{O}_4/\text{Co-Fe}$ LDH core-shell nanowire arrays for high-performance supercapacitor, *Appl. Surf. Sci.* 451 (2018) 280–288.
- H. Pang, Y.-Z. Zhang, Z. Run, W.-Y. Lai, W. Huang, Amorphous nickel pyrophosphate microstructures for high-performance flexible solid-state electrochemical energy storage devices, *Nano Energy* 17 (2015) 339–347.
- B. Senthilkumar, Z. Khan, Park, S. Kim, K. Ko, H.Y. Kim, Highly porous graphitic carbon and $\text{Ni}_2\text{P}_2\text{O}_7$ for a high performance aqueous hybrid supercapacitor, *J. Mater. Chem.* 3 (2015) 21553–21561.
- H. Pang, Z.Z. Yan, W.Q. Wang, Y.Y. Wei, X.X. Li, J. Li, J. Chen, J.S. Zhang, H. H. Zheng, Template-free controlled fabrication of $\text{NH}_4\text{MnPO}_4 \cdot \text{H}_2\text{O}$ and $\text{Mn}_2\text{P}_2\text{O}_7$ micro-nanostructures and study of their electrochemical properties, *Int. J. Electrochem. Sci.* 7 (2012) 12340–12353.
- N.R. Chodankar, D.P. Dubal, S.J. Patil, S.R. Raju, S.V. Karekar, Y.S. Huh, Y.-K. Han, $\text{Ni}_2\text{P}_2\text{O}_7$ micro-sheets supported ultra-thin MnO_2 nanoflakes: a promising positive electrode for stable solid-state hybrid supercapacitor, *Electrochim. Acta* 319 (2018) 435–443.
- C. Chen, N. Zhang, Y.L. He, B. Liang, R.Z. Ma, X.H. Liu, Controllable fabrication of amorphous Co—Ni pyrophosphates for tuning electrochemical performance in supercapacitors, *ACS Appl. Mater. Interfaces* 35 (2016) 23114–23121.
- H. Pang, Z.Z. Yan, Y.H. Ma, G.C. Li, J. Chen, J.S. Zhang, W.M. Du, S.J. Li, Cobalt pyrophosphate nano/microstructures as promising electrode materials of supercapacitor, *J. Solid State Electrochem.* 17 (2013) 1383–1391.
- L.R. Hou, L. Lian, D.K. Li, J.D. Lin, G. Pan, L.Z. Zhang, X.G. Zhang, Q.G. Zhang, C. Z. Yuan, Facile synthesis of $\text{Co}_2\text{P}_2\text{O}_7$ nanorods as a promising pseudocapacitive material towards high-performance electrochemical capacitors, *RSC Adv.* 3 (2013) 21558–21562.
- C. Wei, S. Yang, W. Liu, X. Hou, Y. Sun, J. Zhao, W. Xiong, C. Cheng, D. Zhang, Hierarchically porous bowknot-like sodium doped $\text{Ni}_2\text{P}_2\text{O}_7/\text{Co}_2\text{P}_2\text{O}_7$ with improved supercapacitor performances, *Appl. Surf. Sci.* 465 (2019) 763–771.
- T. Huang, S.K. Moon, J.-M. Lee, A heterostructure of layered double hydroxide wrapped in few-layer carbon with iridium doping for efficient oxygen evolution, *Electrochim. Acta* 296 (2019) 590–597.
- X. Guan, M. Huang, L. Yang, G. Wang, X. Guan, Facial design and synthesis of $\text{CoS}_x/\text{Ni-Co}$ LDH nanocages with rhombic dodecahedral structure for high-performance asymmetric supercapacitors, *Chem. Eng. J.* 372 (2019) 151–162.
- K. Singh, S. Kumar, K. Agarwal, K. Soni, V.R. Gedela, K. Ghosh, Three-dimensional graphene with MoS_2 nanohybrid as potential energy storage/transfer device, *Sci. Rep.* 7 (2017) 9458.
- P. Simon, Y. Gogotsi, Materials for electrochemical capacitors, *Nat. Mater.* 7 (2018) 845–854.
- S.J. Patil, D.W. Lee, Scalable and ascending synthesis of carbon cloth coated hierarchical core-shell $\text{CoMoS}_4/\text{Co}(\text{OH})_2$ for flexible and high-performance supercapacitors, *J. Mater. Chem.* 6 (20) (2018) 9592–9603.
- J. Lin, H. Jia, H. Liang, S. Chen, Y. Cai, J. Qi, C. Qu, J. Cao, W. Fei, J. Feng, Hierarchical $\text{CuCo}_2\text{S}_4/\text{NiMn}$ -layered double hydroxide core-shell hybrid arrays as electrodes for supercapacitors, *Chem. Eng. J.* 336 (2018) 562–569.
- M.W. Su, F. Wu, L. Fang, J. Hu, L. Liu, T. Guan, X. Long, H. Luo, M. Zhou, NiCo-LDH nanowires@nanosheets core-shell structure grown on carbon fiber cloth for high performance flexible supercapacitor electrode, *J. Alloys Compd.* 799 (2019) 15–25.
- J.Q. Sun, W.Y. Li, B.J. Zhang, G. Li, L. Jiang, Z.G. Chen, R.J. Zou, J.Q. Hu, 3D core/shell hierarchies of MnOOH ultrathin nanosheets grown on NiO nanosheet arrays for high-performance supercapacitors, *Nano Energy* 4 (2014) 56–64.
- Y. Zhu, Q. Zong, Q. Zhang, H. Yang, Q. Wang, H. Wang, Three-dimensional core-shell $\text{NiCoP}/\text{NiCoP}$ array on carbon cloth for high performance flexible asymmetric supercapacitor, *Electrochim. Acta* 299 (2019) 441–450.
- H. Rong, T. Chen, R. Shi, Y. Zhang, Z. Wang, Hierarchical $\text{NiCo}_2\text{O}_4/\text{NiCo}_2\text{S}_4$ nanocomposite on Ni foam as an electrode for hybrid supercapacitors, *ACS Omega* 3 (2018) 5634–5642.
- M. Huang, X. Li Zhao, F. Li, W. Li, B. Zhang, Y.X. Zhang, Synthesis of $\text{Co}_3\text{O}_4/\text{SnO}_2/\text{MnO}_2$ core-shell nanostructures for high-performance supercapacitors, *J. Mater. Chem.* 3 (2015) 12852–12857.
- S.J. Patil, J.H. Kim, D.W. Lee, Self-assembled $\text{Ni}_3\text{S}_2/\text{CoNi}_2\text{S}_4$ nanoarrays for ultra high-performance, Supercapacitor, *Chem. Eng. J.* 322 (2017) 498–509.
- Y. Zhang, L. Li, H. Su, W. Huang, X. Dong, Binary metal oxide: advanced energy storage materials in supercapacitors, *J. Mater. Chem.* 3 (2015) 43–59.
- Y.Y. Lan, H.Y. Zhao, Y. Zong, X.H. Li, Y. Sun, J. Feng, Y. Wang, X.T. Zheng, Y.P. Du, Phosphorization boosts the capacitance of mixed metal nanosheet arrays for high performance supercapacitor electrodes, *Nanoscale* 10 (2018) 11775–11781.
- P. Simon, Y. Gogotsi, B. Dunn, Materials science. Where do batteries end and supercapacitors begin? *Science* 343 (6176) (2014) 1210–1211.
- M.R. Lukatskaya, B. Dunn, Y. Gogotsi, Multidimensional materials and device architectures for future hybrid energy storage, *Nat. Commun.* 7 (2016) 12647.
- C. Zhao, Y. Cai, K. Yin, H. Li, D. Shen, N. Qin, Z. Lu, C. Liu, H.-E. Wang, Carbon-bonded, oxygen-deficient TiO_2 nanotubes with hybridized phases for superior Nanion storage, *Chem. Eng. J.* 350 (2018) 201.
- T. Li, J. Wang, Y. Xu, Y. Cao, H. Lin, T. Zhang, Hierarchical structure formation and effect mechanism of Ni/Mn layered double hydroxides microspheres with large-scale production for flexible asymmetric supercapacitors, *ACS Appl. Energy Mater.* 1 (5) (2018) 2242–2253.
- M.-C. Liu, J.-J. Li, Y.-X. Hu, Q.-Q. Yang, L. Kang, Design and fabrication of $\text{Ni}_3\text{P}_2\text{O}_8/\text{Co}_3\text{P}_2\text{O}_8 \cdot 8\text{H}_2\text{O}$ as advanced positive electrodes for asymmetric supercapacitors, *Electrochim. Acta* 201 (2016) 142.
- J.J. Li, M.C. Liu, L.B. Kong, M. Shi, W. Han, L. Kang, Facile synthesis of $\text{Co}_3\text{P}_2\text{O}_8 \cdot 8\text{H}_2\text{O}$ for high-performance electrochemical energy storage, *Mater. Lett.* 161 (2015) 404–407.
- K.V. Sankar, S.C. Lee, Y. Seo, C. Ray, S. Liu, A. Kundu, S.C. Jun, Binder-free cobalt phosphate one-dimensional nanograsses as ultra high performance cathode material for hybrid supercapacitor applications, *J. Power Sources* 373 (2018) 211–219.
- H. Shao, N. Padmanathan, D. McNulty, C. O'Dwyer, K.M. Razeed, Supercapacitor battery based on binder-free $\text{Co}_3(\text{PO}_4)_2 \cdot 8\text{H}_2\text{O}$ multilayer nano/microflakes on nickel foam, *ACS Appl. Mater. Interfaces* 8 (2016) 28592–28598.
- A.A. Mirghani, K.O. Oyedotun, B.A. Mahmoud, A. Bello, S.C. Ray, N. Manyala, Nickel-cobalt phosphate/graphene foam as enhanced electrode for hybrid supercapacitor, *Compos. B Eng.* 174 (2019) 106953.
- Z. Xiao, Y. Bao, Z. Li, X. Huai, M. Wang, P. Liu, L. Wang, Construction of hollow Cobalt–Nickel phosphate nanocages through a controllable etching strategy for high supercapacitor performances, *ACS Appl. Energy Mater.* 2 (2) (2019) 1086–1092.
- B. Liang, Y. Chen, J. He, C. Chen, W. Liu, Y. He, X. Liu, N. Zhang, V.A.L. Roy, Controllable fabrication and tuned electrochemical performance of potassium Co–Ni phosphate microplates as electrodes in supercapacitors, *ACS Appl. Mater. Interfaces* 10 (4) (2018) 3506–3514.
- M. Zhang, J. Sha, X. Miao, E. Liu, C. Shi, J. Li, C. He, Q. Li, N. Zhao, Three-dimensional graphene anchored $\text{Fe}_2\text{O}_3/\text{C}$ core-shell nanoparticles as supercapacitor electrodes, *J. Alloys Compd.* 696 (2017) 956–963.